Indoor Positioning of Autonomous Guided Vehicles Using LiDAR-Corner Cubes with Adaptive Monte Carlo Localization

Pei-Ren Liaw, Brijesh Patel, Ju-Yi Lee, and Po Ting Lin*, Member, RST

Abstract—In the context of Industry 4.0, integrating automation equipment into production lines has become increasingly prevalent. The efficiency of a factory's production is significantly influenced by the autonomous handling and supply of materials or workpieces. This study focuses on the Autonomous Guided Vehicle (AGV) system, which utilizes advanced technologies such as laser optical radar (Light Detection and Ranging, LiDAR) and reflection ridges (Corner Cubes) to achieve indoor positioning and synchronous construction of the contour in a spatial field guided by a specifically dedicated map. The primary emphasis is on AGV indoor positioning technology, employing LiDAR and reflections to calibrate each position coordinate. The research establishes the core technology of indoor Simultaneous Localization and Mapping (SLAM) through the application of a Robots Operating System (ROS), which performs simulation, testing, and the verification analysis of the AGV mechanism. The study also develops a dynamic model for the AGV system, estimates optical position parameters, and integrates them into the Adaptive Monte Carlo Localization (AMCL) combined with the optical indoor positioning algorithm. The hybrid AMCL-Optical positioning provides superior accuracy than individual methods.

Index Terms— Autonomous Guided Vehicle (AGV), Light Detection and Ranging (LiDAR), Corner Cube, Simultaneous Localization And Mapping (SLAM), Indoor Positioning, Adaptive Monte Carlo Localization (AMCL)

I. INTRODUCTION

In recent decades, significant technological advancements have propelled us into an era marked by automation and the integration of data exchange processes within manufacturing domains recognized as Industry 4.0 [1]. At its core, Industry 4.0

Manuscript received 21 December 2023; accepted 11 January 2024; date of publication 18 January 2024. This paper was supported by the National Science and Technology Council (NSTC), Taiwan (Grant No: NSTC 112-2811-E011-032, NSTC 112-2218-E-011-009), and the Intelligent Manufacturing Innovation Center (IMIC) at the National Taiwan University of Science and Technology, Taipei, Taiwan

Pei-Ren Liaw was a MS students in Department of Mechanical Engineering at National Taiwan University of Science and Technology (NTUST), Taipei, Taiwan. (e-mail: jen225668@gmail.com)

Brijesh Patel is a Postdoctoral Researcher in Department of Mechanical Engineering at National Taiwan University of Science and Technology (NTUST), Taipei, Taiwan. (e-mail: aero.brijesh@gmail.com)

Ju-Yi Lee is a Professor in Department of Mechanical Engineering at National Central University (NCU), Taoyuan, Taiwan. (e-mail: juvilee@cc.ncu.edu.tw)

Po Ting Lin is a Professor in Department of Mechanical Engineering and Intelligent Manufacturing Innovation Center (IMIC) at National Taiwan University of Science and Technology (NTUST), Taipei, Taiwan. (Corresponding author. phone: +886-983-033-147; e-mail: potinglin@mail.ntust.edu.tw)

envisions a production landscape where humans and machines collaborate within a cyber-physical system, fostering communication, cooperation, and self-organization [2]. A pivotal aspect of Industry 4.0 is the emphasis on Human-Robot Collaboration (HRC), where collaborative robots, or cobots equipped with safety and collision avoidance systems, work alongside human counterparts without the need for additional safety barriers [3]. In cutting-edge intelligent unmanned factories, common automated handling systems include automated guided vehicles (AGVs) [4], and autonomous mobile robots (AMRs) [5]. The advent of Industry 4.0 has fueled a growing demand for customization. AGVs, being programmable for route planning and task automation, excel in scenarios requiring frequent changes in handling paths. The dynamic nature of customization necessitates rapid advancements in intelligent positioning, mapping, and navigation technologies for AGVs [6], making them pivotal in contemporary robotics and autonomous unmanned vehicles. Within this framework of industry 4.0 and HRC, a reliable Indoor Positioning System (IPS) is crucial for indoor transportation, facilitating navigation, and pinpointing the locations of individuals, robots, and autonomous vehicles [7, 8]. IPS plays a key role in realizing the full potential of Industry 4.0 in contemporary production plants.

In autonomous guided vehicles (AGVs), acquiring real-time environmental information and precise location data is crucial for ensuring safe and efficient movement. To achieve this, having an accurate map of the environment and the AGV's positioning information is imperative. The evolution of technologies like wireless networks and mobile computing has led to the increasing popularity of location positioning [9]. While the Global Positioning System (GPS) [10] excels in outdoor settings, it falls short for indoor positioning due to poor satellite signal penetration. Indoor positioning, essential in various settings such as factories, airports, and exhibitions, faces the challenges of environmental interference and higher accuracy requirements. As a result, indoor positioning has become a prominent research focus in the broader field of positioning and navigation.

Commercial indoor mapping systems featuring LiDAR or RGB-D cameras share common components for data processing and sensor synchronization [11]. Complementary sensors like RGB cameras or thermographic sensors may be added for enhanced data acquisition. Unlike outdoor devices using GNSS signals, indoor systems address signal penetration challenges through inertial methods, beacons, or, commonly

[12], SLAM algorithms initially developed for autonomous robots[13].

This study presents a novel indoor positioning method for automatic guided vehicles, utilizing LiDAR and Corner Cube optical features to overcome featureless environments. The approach integrates the AMCL algorithm to compensate for AGV positioning errors and ensure continuous and accurate tracking. Implemented in the Robot Operating System (ROS), the method is validated through preliminary simulations and analyses using the OmniBot automated guided vehicle system.

II. REVIEW ON EXISTING INDOOR POSITIONING AND MAPPING TECHNIQUES.

The literature reveals a growing emphasis on robot Indoor Positioning Systems (IPS) to ascertain real-time positions within designated workspaces. Fig. 1 shows different types of techniques and methods for IPS. Accurate indoor robot localization is crucial, but traditional methods like GPS fall short indoors due to signal blockage [14]. Recent research has leveraged ubiquitous Wi-Fi signals [15] for cost-effective and accessible indoor robot positioning, avoiding the need for additional infrastructure compared to other technologies like Bluetooth[16], Infrared[17], and UWB [18]. Many techniques have been explored to address indoor robot localization, with a focus on the simultaneous localization and mapping (SLAM) problem. LiDAR sensors, with active light, provide precise and dense environmental data, especially in fast-moving indoor settings, ensuring robust localization with SLAM systems [19]. Yang et al. propose a pixel threshold eight-point method and an improved epipolar constraint algorithm to enhance the accuracy of vision-based indoor positioning, offering a cost-effective solution additional hardware [20].

Robot Indoor Positioning Techniques Wireless Communication Map Matching Equipment /Self Positioning Positioning Positioning Bluetooth LiDAR Global Infrared Camera Kidnapping Problem WLAN UWB Tracking ZigBee

Fig. 1. Robot indoor positioning methods

Various methods have been explored in the literature, as documented in works such as shown in Fig. 2 [21, 22].

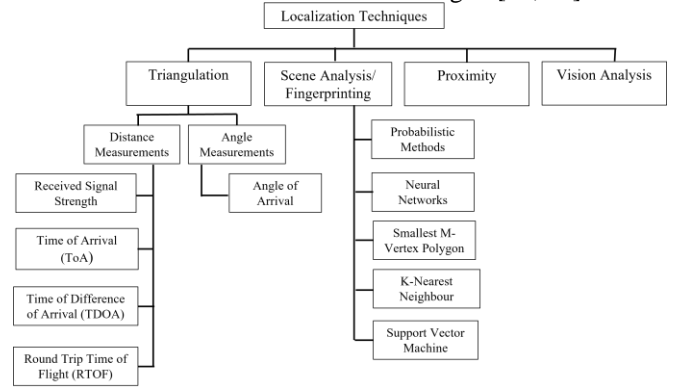


Fig. 2. IPS localization techniques and methods [22]

Triangulation, as highlighted, utilizes the geometric properties of triangles to calculate an object's position based on known reference point coordinates [23]. Notable algorithms, including Received Signal Strength Indicator (RSSI), Angle of Arrival (AOA), Time of Arrival (TOA), Time Difference of Arrival (TDOA), and Time of Flight (TOF), are widely employed [24, 25]. RSSI utilizes signal strength attenuation [26], while AOA calculates angles for precise positioning. TOA relies on time calculations, requiring accurate synchronization, and **TDOA** employs hyperbolic characteristics [27]. TOF measures the time difference between transmitted and received pulses.

Fingerprinting involves an offline stage where a feature database is established and an online stage where measured features are compared for location estimation [28]. Adege et al. propose a system for both indoor and outdoor positioning; the work utilizes a hybrid of Support Vector Machine and Deep Neural Network algorithms [29]. In a different approach to indoor positioning, Malar et al. suggest an indoor positioning system based on fingerprinting and support vector machines [30]. Additionally, Zheng et al. introduced an indoor localization system employing a particle filter and support vector machine. This system aims to determine the user's speed and direction of motion through a mobile device, leveraging the device's sensors and utilizing a particle filter for effective sensor fusion [31].

Proximity-based systems, relying on grids of antennas with known locations, detect an object's position based on its proximity to these antennas [32]. Vision analysis, a technique rooted in image processing by cameras covering the indoor environment, identifies predefined objects within a database [33].

III. MATERIAL AND METHODS

A. LiDAR-SLAM

This study utilizes the PEPPERL+FUCHS LiDAR model OMD30M-R2000-B23-V1V1D-HD-1L manufactured Germany. This LiDAR offers an impressive specification, including a 360° detection range, a 30m detection distance, ±25mm absolute accuracy, and ±12mm measurement noise. Renowned for its high precision and stability, this LiDAR is well-suited for Autonomous Guided Vehicle (AGV) operations and diverse application environments due to its resistance to background interference and strong anti-ambient light capabilities. Operating on Pulse Ranging Technology (PRT) and following the Time of Flight (TOF) principle, the LiDAR calculates target distance based on the time difference between pulse transmission and reception, offering resilience to external light sources and minimal sensitivity to environmental changes. Additionally, it incorporates a sophisticated filtering algorithm with three variations—average/mean, maximum value, and reflected energy—tailored for noise reduction, challenging conditions, and low reflectivity, respectively. The LiDAR's adaptability is further enhanced by its compatibility with PACTware DTM series components, known for their user-friendly interface, facilitating easy setup and operation. This comprehensive LiDAR solution generates indoor contour graphics, showcasing its robust capabilities in various scenarios.

In this study, the Gmapping SLAM [34], a widely used approach for lidar and odometry, employs Rao-Blackwellized Particle Filters (RBPF) method with enhancements. In the RBPF algorithm, particles are strategically placed on the map, assigned different weights based on sensor values, and selectively retained or removed. The RBPF-based SLAM process involves sampling, importance weighting, adaptive resampling, and map estimates. Particles are drawn based on an initial pose estimate from a motion model and refined using the latest observations. Importance weighting evaluates how well particles represent the target distribution. Adaptive resampling may be triggered based on the effective particle number. Finally, the map carried by each particle is updated through the robot's pose history and observations. Gmapping improves the proposal distribution and selective resampling, providing accurate mapping in long corridors and low-feature environments. However, it relies on odometer data and is unsuitable for uneven ground or drone applications.

B. Corner Cube

The Corner Cube is an optical pyramid reflector composed of three-sided glass prisms that redirect the incident beam in the opposite direction. It is commonly used in measurement and laser light-ranging applications. This experiment employed the product prism with corner pyramid specifications D12.7*9.5 mm provided by Yugun Optoelectronics Technology Co., Ltd. The working principle of the Corner Cube involves three reflections, once from each surface, causing a reversal in the direction illustrated in Fig. 3. The Corner Cube features three perpendicular faces forming a Cartesian coordinate system (x, y, z), with [a,b,c]representing the direction of any incident As the incident light rays reflect successively from different sides of the Corner Cube, specific changes occur in their directional components. Initially, when reflected from the first side, the x-component, denoted as 'a' undergoes reversal to -a', while the y and z-components remain unaltered, resulting in a modified direction of [-a,b,c]. Similarly, upon reflection from the y and z sides, the b and c components undergo a reversal. The sequential reflections result in the ray direction transitioning through [a,b,c] to [-a,b,c], then to [-a,-b,c]finally to [-a,-b,-c], and ultimately departing from the Corner Cube. Notably, the distance traveled remains constant for any incident ray, irrespective of its initial reflection point.

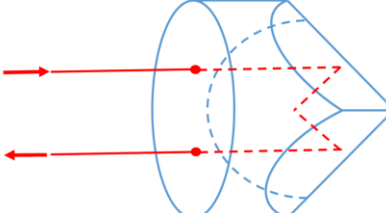


Fig. 3. Schematic diagram of corner cube

C. ROS-Gazeebo

The Robot Operating System (ROS) is an open-source meta-operating system designed for robot software development, offering services akin to an operating system. It facilitates hardware abstraction, low-level device control, implementation of common functionalities, and inter-process message passing. ROS operates as a peer-to-peer process network during runtime, utilizing a communication infrastructure for loose coupling. ROS adopts a distributed processing architecture with nodes, emphasizing code reuse, enabling independent design and flexible coupling at runtime. It encourages clear function interfaces for writing ROS-agnostic libraries, supporting collaboration through distributed code repositories. The detailed ROS architecture is illustrated in Fig. 4.

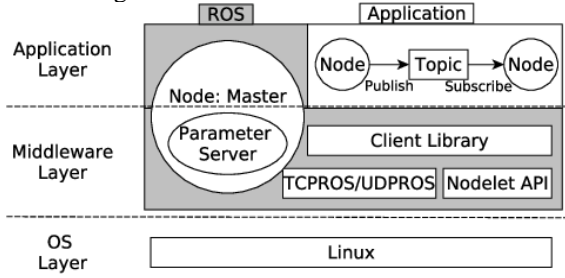


Fig. 4. ROS architecture

In terms of system modeling and configuration, the study employs standard ROS tools like Gazebo, Rviz, and rqt for visualization. Gazebo, a 3D robot simulator, is used to create a simulation environment for AGV, importing the robot using the Unified Robot Description Format (URDF). Rviz serves as a 3D parameter visualization tool with plugins for importing maps and displaying sensor data. The rqt tool, a graphical user interface, visualizes AGV's standalone runtime. The TF (Transformation) system in ROS allows practical visualization of coordinate transformations, which is essential for understanding relationships between different coordinate systems. Together, these tools enhance ROS's capabilities, providing a comprehensive framework for effective robot research and development.

D. Adaptive Monte Carlo Positioning (AMCL)

Monte Carlo localization (MCL) [35] is an algorithm employing a particle filter for a robot to estimate its position and orientation while navigating and sensing the environment with a given map. In MCL, particles represent potential robot states $X = (X, Y, \theta)$, initially uniformly distributed across the environmental state space, indicating a lack of prior global positioning information. As the robot moves and senses the surroundings, particles undergo resampling based on sensor observations to converge toward the actual pose state. In each iteration, the robot undergoes motion updates, applying the robot's movement to all particles. Sensor updates refine particle positions based on the robot's environment sensing, adjusting particle weights to enhance accuracy. Resampling generates a new set of particles around those with higher weights, optimizing computational resources. The MCL algorithm is shown below:

- 1 Algorithm $MCL(X_{t-1}, u_t, z_t)$:
- $\overline{X}_{t} = X_{t} = \emptyset$
- 3 for m=1 to M:
- $x_{t}^{[m]} = motion_update(u_{t}, x_{t-1}^{[m]})$
- $w_{t}^{[m]} = sensor_update(z_{t}, x_{t}^{[m]})$
- $\overline{X}_{t} = \overline{X}_{t} + \langle x_{t}^{[m]}, w_{t}^{[m]} \rangle$

- 7 end for
- 8 for m = 1 to M:
- 9 draw $x_t^{[m]}$ from \overline{X}_t with probability $\propto w_t^{[m]}$
- 10 $X_{\cdot} = X_{\cdot} + x_{\cdot}^{[m]}$
- 11 end for
- 12 return X,

Monte Carlo Localization (MCL) starts with a large number of evenly distributed particles on the map, but over iterations, they cluster in one location, wasting computational resources if the initial count is maintained. Adaptive Monte Carlo Localization (AMCL) [36] improves MCL by dynamically adjusting particle numbers using the Kullback-Leibler Divergence (KLD) method [37]. AMCL addresses MCL's computing inefficiency by recalculating the particle count in each iteration, eliminating redundant particles for improved performance. AMCL's adaptation resolves fixed particle count issues and mitigates the problem of robot kidnapping by adjusting particle numbers based on localization accuracy.

E. Indoor Localization Algorithm Design

This study integrates the optical positioning method and the AMCL positioning method for indoor positioning. The goal is to address the limitations of both the AMCL global positioning and indoor optical methods. The aim is to enhance the efficiency of AGV indoor positioning tasks in environments with similar spatial geometry or large areas.

Basically, the concept of indoor optical positioning for the AGV on-board system in this paper involves constructing the position coordinates $P_{S,i}(X_i,Y_i)$ for S=4 optical reflective prisms (Corner Cube) detection points in the indoor geographic coordinate system, where $i=1,2,...,N_S$. The LiDAR is employed to measure the distance L_{LSi} between these detection points, as represented by Eq. (1). Convert back to the LiDAR measurement position coordinates $P_{LD}(X,Y)$. The LiDAR coordinate point is P_{LD} ; the optical reflective prism coordinate point is P_{Si} .

$$L_{LSi} = \left\| P_{LD} - P_{s,i} \right\| \tag{1}$$

In 3D spatial coordinates, distance is a scalar quantity. The distance between LiDAR and each optical reflecting prism is accurately estimated using Bier's theorem. The derivation process involves applying the polygon positioning principle and the three-point ranging formula. The AGV on-board system operates in inertial coordinates $O_G - X_E Y_N Z$, assuming a constant height for the LiDAR and all reflecting prism points $Z = z_i$. This simplification to the 2D XY plane motion allows for spatial distance calculations using Bier's theorem. The coordinates of the LiDAR detection point and the selected prism reflection point denoted $P_{S,i}(X_i, Y_i)$ and $P_{S,j}(X_j, Y_j)$ respectively, with their square distance given by Eq. (2) and Eq. (3).

$$L_{i}^{2} = (X - X_{i})^{2} + (Y - Y_{i})^{2}$$
 (2)

$$L_{L_j}^2 = (X - X_j)^2 + (Y - Y_j)^2$$
 (3)

After resolving the Eq. (2) and (3),

$$L_{Li}^2 - L_{Li}^2 = [(X - X_i)^2 + (Y - Y_i)^2] - [(X - X_i)^2 + (Y - Y_i)^2]$$
 (4)

$$L_{L_i}^2 - [(X^2 + X_i^2 - 2XX_i) + (Y^2 + Y_i^2 - 2YY_i)]$$

= $L_{L_j}^2 - [(X^2 + X_j^2 - 2XX_j) + (Y^2 + Y_j^2 - 2YY_j)]$ (5)

Eq. (5) can be simplified as,

$$L_{Li}^{2} - (X^{2} + Y^{2}) + (X_{i}^{2} + Y_{i}^{2}) - 2[XX_{i} + YY_{i}]$$

$$= L_{L}^{2} - (X^{2} + Y^{2}) + (X_{j}^{2} + Y_{j}^{2}) - 2[XX_{j} + YY_{j}]$$
(6)

In Eq.(6), specify the focal point of reflection prisms i and j as $P_{S,i}(X_i,Y_i)$ and $P_{S,j}(X_j,Y_j)$, respectively. Define the distance between the coordinate origin O(0,0) and the prisms using Eq. (6). After horizontally shifting the items, rearrange and rewrite the Eq. (7).

$$L_{L_i}^2 - (X_i^2 + Y_i^2) - L_{L_j}^2 - (X_j^2 + Y_j^2)$$

$$= 2X(X_i - X_j) - 2Y(Y_i - Y_j)$$
(7)

Assuming there are m groups of reflection prisms, the LiDAR measures the test distance value for each group per scan, denoted L_{Li} , i=1,2,...,m. Equation (7) is expressed on both sides of the equal sign, as shown in Eq (8) and (9).

$$A_{k} = L_{Li}^{2} - (X_{i}^{2} + Y_{i}^{2}) - L_{Li}^{2} - (X_{i}^{2} + Y_{i}^{2})$$
 (8)

$$B_{k,1} = 2(X_i - X_j), B_{k,2} = -2(Y_i - Y_j)$$
(9)

Where k = 1, 2, ..., m. The above Eq (8) and (9) is a group of m simultaneous linear equations, which is rewritten into matrix form, as in Eq. (10).

$$A = BP, \text{ where A} = \begin{bmatrix} A_1 \\ A_2 \\ . \\ . \\ A_m \end{bmatrix}, B = \begin{bmatrix} B_{11} & B_{12} \\ B_{21} & B_{22} \\ . & . \\ . & . \\ B_{m1} & B_{m2} \end{bmatrix}, P = \begin{bmatrix} X \\ Y \end{bmatrix}$$
(10)

A is a $[m \times 1]$ matrix, B is a $[m \times 2]$ matrix, and P is a $[2 \times 1]$ matrix. Solving for the position vector P involves setting Eq. (10) equal on both sides and left multiplying by the transpose matrix. This results in the $[B^TB]$ $[m \times m]$ square, as shown in Eq. (11).

$$B^T A = B^T B P \tag{11}$$

Given the known spatial coordinates of the indoor optical reflectance prism, LiDAR scanning is employed to derive the relative distance test value. This process results in the formulation of an approximate linear system representing AGV distance measurement and coordinate position, expressed in Eq. (12) to Eq. (14).

$$A = BP, \text{ where A} = \begin{bmatrix} A_1 \\ A_2 \\ . \\ . \\ A_m \end{bmatrix}, B = \begin{bmatrix} B_{11} & B_{12} \\ B_{21} & B_{22} \\ . & . \\ . & . \\ B_{m1} & B_{m2} \end{bmatrix}, P = \begin{bmatrix} X \\ Y \end{bmatrix}$$
 (12)

$$A_k = \{L_{LSi}^2 - (X_{Si}^2 + Y_{Si}^2)\} - \{L_{LSi}^2 - (X_{Si}^2 + Y_{Si}^2)\}$$
 (13)

$$B_{k,1} = 2(X_{si} - X_{si}), B_{k,2} = -2(Y_{si} - Y_{si})$$
 (14)

Where k = 1, 2, ..., m, and to solve the linear system Eq. (12), let $[B^T B]$ is a square matrix of $[m \times m]$ as in Eq. (15),

$$B^T A = B^T B P \tag{15}$$

The numerical solution for the LiDAR position vector $P_{LD}(X,Y)$ is obtained, as depicted in Eq. (16).

$$P = (B^T B)^{(-1)} B^T A (16)$$

Minimize the sum of squares of measurement errors using numerical solutions, as defined by Eq. (17),

$$Min(Squre Error) = Min([B^{T}(A-BP)]^{2})$$
 (17)

Minimizing LiDAR measurement errors is achieved by determining the position vector $P_{LD}(X,Y)$ through Eq. (17). To find the optimal solution for the system $P_{LD}(X_o,Y_o)$, simultaneous equations are solved, subject to mathematical constraints specified in Eq. (18).

$$\left\{ \frac{\partial [B^{T}(A - BP)]^{2}}{\partial X} \Big|_{X = X_{0}} = 0 \\
\frac{\partial [B^{T}(A - BP)]^{2}}{\partial Y} \Big|_{Y = Y_{0}} = 0
\right.$$
(18)

The known spatial coordinates of indoor optical reflectance prisms, denoted as $P_{S,i}(X_{Si},Y_{Si})$, are assumed to undergo LiDAR scanning to obtain relative distance test values, L_{DSi} , which are treated as random variables subject to random error distribution. Here, i represents the sample point code, ranging from $i=1,2,...,N_S$. The experiment involves stratified sampling for the four Corner Cubes test positions (S=4). The distance test value L_{DS} , is treated as a random variable with a normal distribution function, $N(L_{DS} | \mu_S, \sigma_S^2)$ represented by a Gaussian probability density function, as given in Eq. (19),

$$N(L_{DS} \mid \mu_{S}, \sigma_{S}^{2}) = \frac{1}{\sqrt{2\pi\sigma_{s}}} e^{-\frac{(L_{DS} - \mu_{S})^{2}}{2\sigma_{S}^{2}}}$$
(19)

Where S=1,2,3,4.

IV. EXPERIMENT DESIGN OF INDOOR OPTICAL POSITIONING

A. Experimental Design of Indoor Positioning Using LiDAR

This study explores LiDAR and Corner Cube applications in indoor positioning and simultaneous contour mapping (SLAM). Preliminary experiments involve indoor mapping, positioning, and distance measurements for AGV tracking. LiDAR and Corner Cube are positioned in a fixed room with known maps, conducting static distance tests and contour mapping with varying sample sizes. The aim is to validate LiDAR's ranging function and accuracy, assess the impact of sample size on distance measurement accuracy ($N_{S1} = N_{S3} = 50, N_{S2} = N_{S4} = 500$), and discuss positioning result consistency through statistical estimation.

As depicted in Fig. 5, the LiDAR is fixed on the indoor ground, while four reflective prism Cubes are positioned on the thin plate wall around the room. The exterior space dimensions in Case 1.1 and Case 1.2 are W=1700mm, L=2900mm, forming a polygonal area. The position coordinates (mm) are LiDAR Pxy=[15, -165], Corner Cube [S1;S2;S3;S4] = [-650, 0; 0, 850; 1000, 0; 0,-2000]. For Case 2.1 and Case 2.2, the experimental site maintains the same scene layout with LiDAR coordinates Pxy=[20, -5] and Corner Cube [S1;S2;S3;S4]= [-650, 0; 0, 850, 0; 1000, 0; 0, -2000].

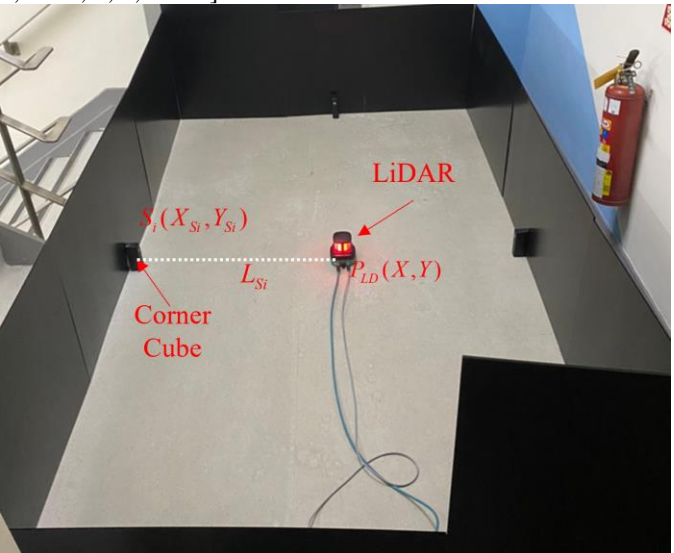
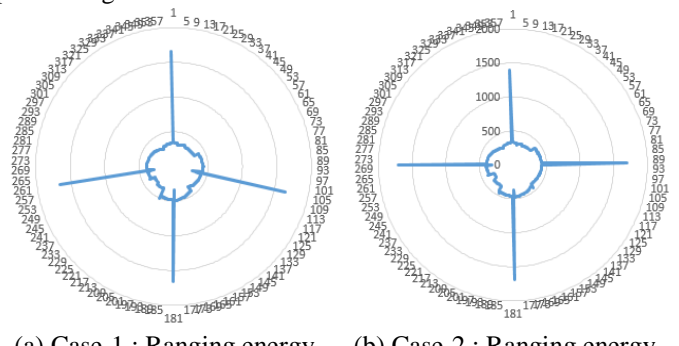


Fig. 5. Layout of the indoor test space for LiDAR experiments

B. Contour Map Creation

The experimental setup involved planning the test site, arranging LiDAR and Cube test equipment, and conducting indoor optical positioning experiments. LiDAR scanned and measured distances to each Cube, generating a radar map of reflected echo energy as shown in Fig. 6. The digitized values of the environment contour were then used to create an indoor contour map as shown in Fig. 7, providing AGV on-board systems with boundary information for autonomous positioning.



(a) Case-1 : Ranging energy responds to LiDAR maps responds to LiDAR charts Fig. 6. LiDAR/Cube indoor scanning and positioning data

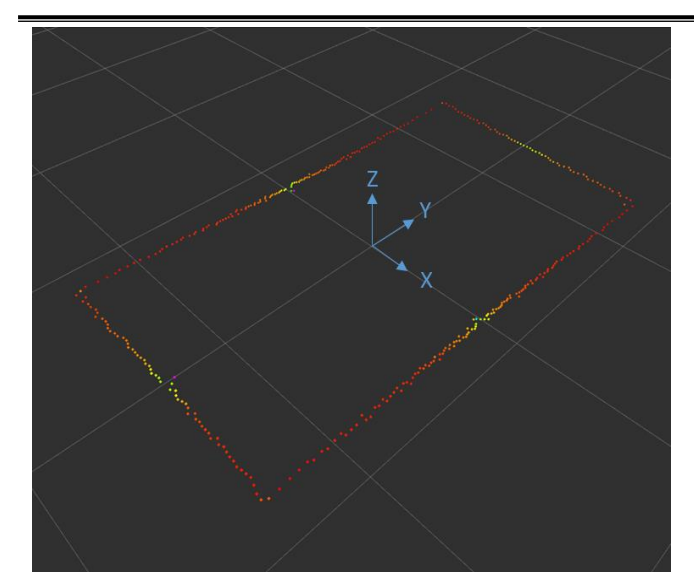


Fig. 7. Indoor space boundary outline map

C. LiDAR test data and its analysis

The test revealed that in the absence of occlusions between the LiDAR scanning beam and optical prisms, accurate coordinate estimation was achieved. Despite the LiDAR being stationary, the laser pulse wave energy response from four reflective prisms on the indoor wall was distinct. The pulse wave reflected at various locations resulted in a spectrum of relative distances with random variations, representing the ranging system's uncertainty or accuracy. MATLAB® was employed for statistical analysis, utilizing distance values to implement a 2-D three-point positioning and linear least squares algorithm for LiDAR position coordinates $P_{LD}(X,Y)$.

In this experiment, LiDAR is equipped with four optical reflection prisms with well-defined spatial coordinates. LiDAR scans yield a statistical probability distribution for the measured distance-random variable, L_{DSi} , stratified into S layers. In this experiment, with S=4 and sample sizes ($N_{S1}=50, N_{S2}=500, N_{S3}=50, N_{S4}=500$) assumed to follow a normal distribution $N(\mu_{Si}, \sigma_{Si})$.

Experimental design involved $N_{SP1} = 50$ and $N_{SP2} = 500$ samples, estimating normal distribution statistics (μ_S, σ_S) for random variables, as detailed in Table. 1. The LiDAR/Cubes ranging result data, $P_{LS}(X,Y)$, and positioning estimates distribution are illustrated in Fig. 8 to Fig. 11, with an enlarged view of LiDAR position attitude coordinates, $P_{LD}(X,Y)$ regions on the right. Statistical analysis results for the experimental distance values between LiDAR and Cubes S (S=1,2,3,4), L_{DSI} , are summarized in Table. 2.

Case 1.1 involves the LiDAR and Corner Cube positional coordinates, a sample population denoted as L_{DSi} , with i ranging from 1 to 50 and S from 1 to 4. The minimum standard deviation of the sample, $L_{\sigma S}$, is 7.12 @ L_{D4} , while the maximum is 9.06 mm@ L_{D3} . Notably, Cube 4 exhibits the lowest sample population error, whereas Cube 2 has the highest.

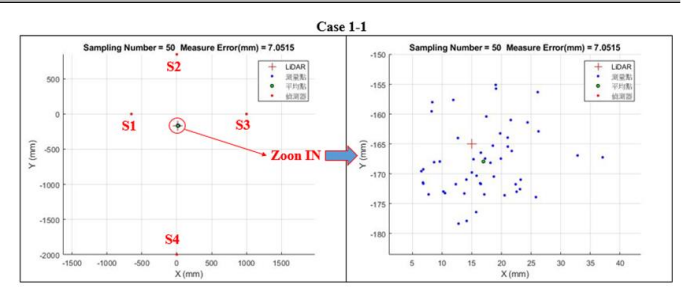


Fig. 8. Spatial distribution of LiDAR/Cubes ranging data positioning estimates for case 1.1

Case 1.2 is identical with case 1.1 for position coordinates a sample population denoted as L_{DSj} , with j ranging from 1 to 500 and S from 1 to 4 The minimum standard deviation of the sample, $L_{\sigma S}$, is 7.59 mm observed at L_{D4} , while the maximum is 9.76 mm at L_{D1} . Cube 4 demonstrates the lowest sample population error, whereas Cube 2 has the highest.

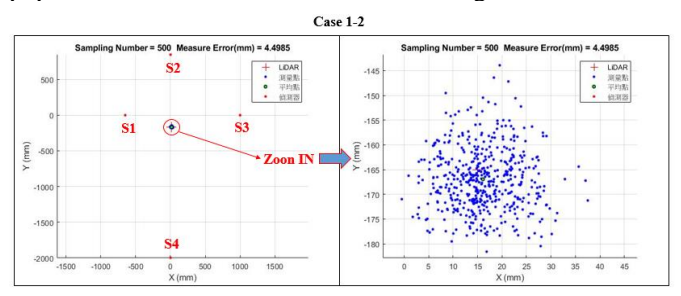


Fig. 9. Spatial distribution of LiDAR/Cubes ranging data positioning estimates case 1.2

Case 2.1 assigns the LiDAR and Corner Cube positional coordinates, a sample population denoted as L_{DSi} , with i ranging from 1 to 50 and S from 1 to 4. The minimum standard deviation of the sample, $L_{\sigma S}$, is 6.65 mm @ L_{D4} , while the maximum is 10.55 mm@ L_{D1} . Notably, Cube 4 exhibits the lowest sample population error, whereas Cube 2 has the highest.

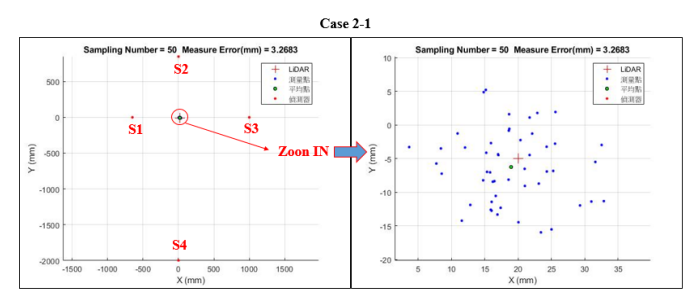


Fig. 10. Spatial distribution of LiDAR/Cubes ranging data positioning estimates case 2.1

Case 2.2 is identical with case 2.1 for position coordinates a sample population denoted as L_{DSj} , with j ranging from 1 to 500 and S from 1 to 4 The minimum standard deviation of the sample, $L_{\sigma S}$, is 6.90 mm observed at L_{D4} , while the maximum is 9.90 mm at L_{D1} . Cube 4 demonstrates the lowest sample population error, whereas Cube 2 has the highest.

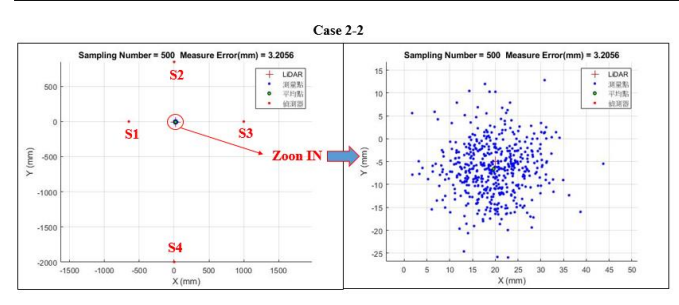


Fig. 11. Spatial distribution of LiDAR/Cubes ranging data positioning estimates case 2.2

Table. 1. Statistics of LiDAR/Cubes ranging data

| Table. 1. Statistics of LiDAN/Cubes ranging data | | | | | | |
|--|-----------------------------|-----------------------------------|-------------|----------|----------------|--|
| Cube | $L_{\scriptscriptstyle DS}$ | $L_{\scriptscriptstyle DS}$ | $L_{\mu S}$ | E_{rs} | $L_{\sigma S}$ | |
| S | (mm) | (mm) | (mm) | (mm) | (mm) | |
| Case 1.1: | | No of Samples (N_{SPn}) = 50 | | | | |
| 1 | $L_{_{\mathrm{1}D1}}$ | 685.2 | 669.7 | 15.5 | 8.92 | |
| 2 | $L_{_{1D2}}$ | 1015.1 | 966.8 | 48.3 | 7.56 | |
| 3 | $L_{_{1D3}}$ | 998.7 | 978.5 | 20.2 | 9.06 | |
| 4 | $L_{_{1D4}}$ | 1835.1 | 1815.6 | 19.5 | 7.12 | |
| Case 1.2 : | | No of Samples (N_{SPn}) = 500 | | | | |
| 1 | L_{2D1} | 685.2 | 666.9 | 18.3 | 9.76 | |
| 2 | L_{2D2} | 1015.1 | 967.2 | 47.9 | 8.31 | |
| 3 | L_{2D3} | 998.7 | 978.5 | 20.2 | 8.33 | |
| 4 | L_{2D4} | 1835.1 | 1816.6 | 18.5 | 7.59 | |
| Case 2.1: | | No of Samples (N_{SPn}) = 50 | | | | |
| 1 | L_{3D1} | 670.0 | 646.6 | 23.4 | 10.55 | |
| 2 | $L_{_{3D2}}$ | 855.2 | 809.0 | 46.2 | 8.99 | |
| 3 | L_{3D3} | 980.0 | 961.8 | 18.2 | 8.05 | |
| 4 | L_{3D4} | 1995.1 | 1980.7 | 14.4 | 6.65 | |
| Case 2.2 : | | No of Samples (N_{SPn}) = 500 | | | | |
| 1 | L_{3D1} | 670.0 | 648.7 | 21.3 | 9.90 | |
| 2 | L_{3D2} | 855.2 | 809.4 | 45.8 | 8.43 | |
| 3 | $L_{_{3D3}}$ | 980.0 | 961.9 | 18.1 | 8.17 | |
| 4 | L_{3D4} | 1995.1 | 1980.6 | 14.5 | 6.90 | |

Table. 2. Statistical Analysis of Estimated LiDAR Location Coordinates (X, Y)

| Case | No of Sample N_{SPn} | True Value $X_n (mm)$ | Average Value X $\mu_n(mm)$ | Standard Deviation $X\sigma_n(mm)$ |
|------|------------------------|--------------------------------------|--|---|
| 1.1 | 50 | 15 | 16.97 | 6.71 |
| 1.2 | 500 | 15 | 16.09 | 6.60 |
| 2.1 | 50 | 20 | 18.94 | 6.45 |
| 2.2 | 500 | 20 | 19.66 | 6.20 |
| | No of | True | Average | Standard |
| Case | Sample N_{SPn} | Value Y _n (mm) | Value Yµ _n (mm) | Deviation $Y\sigma_n$ (mm) |
| Case | Sample | Value | Value | Deviation |
| | Sample N_{SPn} | Value Y _n (mm) | Value Yµ _n (mm) | $\begin{array}{c} Deviation \\ Y\sigma_n (mm) \end{array}$ |
| 1.1 | Sample N_{SPn} 50 | Value Y _n (mm) -165 | Value Yμ _n (mm) -167.93 | Deviation $Y\sigma_n$ (mm) 5.76 |

Utilizing LiDAR/Cubes ranging data, the three-point positioning and least squares (LSQ) algorithm were employed to derive statistical estimates of LiDAR position coordinates (X, Y).

- Case 1.1 Positioning Error: 7.05mm.
- Case 1.2 Positioning Error: 4.50mm.
- Case 2.1 Positioning Error: 3.27mm.
- Case 2.2 Positioning Error: 3.21mm.

Results from Case 1 and Case 2 indicate that optimal positioning accuracy is achieved when the LiDAR position is perpendicular to the corner cube. Sample size minimally affects positioning accuracy. In cases where the LiDAR and corner cube have an angled irradiation angle, positioning accuracy slightly diminishes in experiments with a small number of samples but remains within an acceptable range

D.AMCL integrated with optical indoor positioning method simulation.

Integrating AMCL with optical positioning techniques exhibits a unique strength. Combining these methods addresses potential reliability issues that may arise when each method is used separately. AMCL can face challenges in environments with highly repetitive geometric features, leading to positioning failures. On the other hand, optical positioning may encounter failures or inaccuracies due to obstacles or angles. By integrating both approaches, the environmental features captured by optical positioning can enhance AMCL's particle convergence speed and overall positioning reliability. The experiment involves two stages: first, using SLAM for map construction, coordinate system definition, and optical prism position recording; second, employing the constructed map for AGV's indoor global positioning, enhancing overall accuracy and reliability. In this experiment, Gmapping SLAM in ROS constructed the simulation map using two environments in Gazebo with the AGV model. The node graph was checked by SLAM to understand the sensor information flow direction. The SLAM results were observed using Rviz, simulating a rectangular environment map with low and high features, as depicted in Fig. 12.





Fig. 12. Rectangular environment map with low features

In this experiment, the focus shifted to the indoor global positioning of the Omnibot AGV, utilizing the map constructed in the previous stage. The convergence of particle numbers was observed by implementing both the traditional AMCL positioning method and the AMCL combined with optical positioning. The experiment involved calculating the error between the actual AGV position and the positioning result. A comparative analysis was conducted between the positioning outcomes of the traditional AMCL method and the AMCL

combined with optical positioning. Fig. 13 visually depicts the key stages of the experimental process.

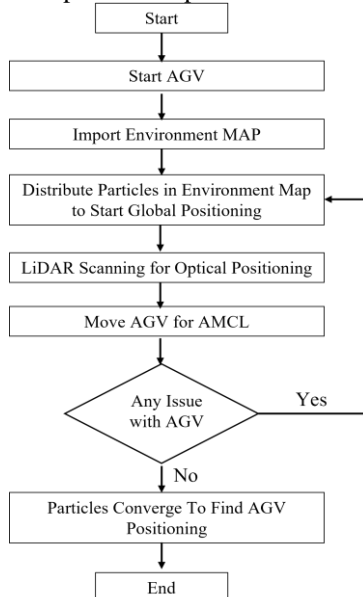
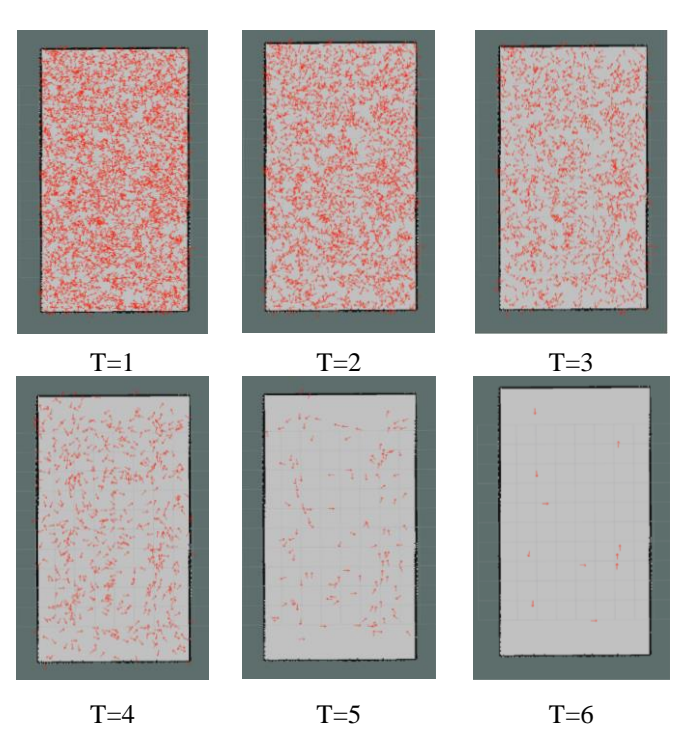


Fig. 13. Flow diagram of the experimental process 1) Traditional AMCL method

The simulation experiment utilized the traditional AMCL localization method, as depicted in Fig. 14, showcasing the particle distribution at nine distinct time points. Given the absence of initial pose information from LiDAR alone, the particles are uniformly distributed across the map. The convergence process of particle numbers is driven by both motion and sensor information. The positioning error, calculated by comparing the actual AGV posture with the estimated posture of AMCL at each time point, reveals the variations in positioning error at nine different instances, as depicted in Fig. 15.



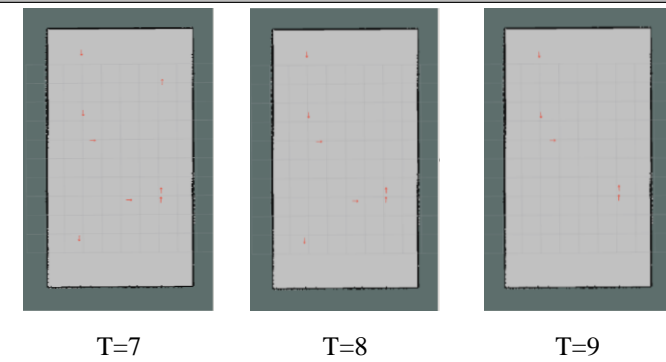


Fig. 14. Particle distribution map of traditional AMCL positioning (simulation)

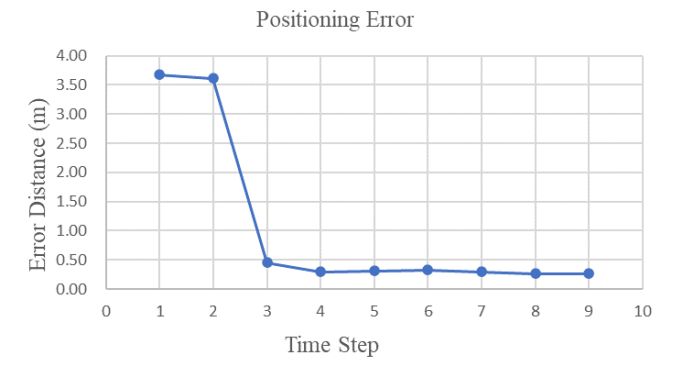
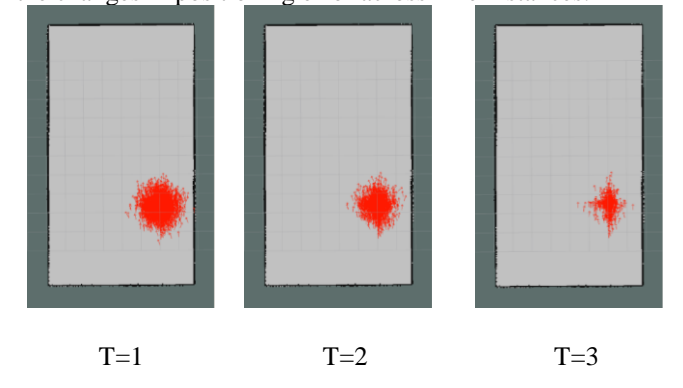


Fig. 15. Traditional AMCL positioning error plot 2) AMCL combined with optical method

In this simulation experiment, the methodology involves combining AMCL with the optical positioning method. Fig. 16 displays the particle distribution at nine specific instances, showcasing the AGV's ability to establish the initial possible pose information distribution range through the optical positioning method. The particles initially exhibit a more concentrated distribution with optical localization and gradually converge through movement and sensor information to achieve accurate positioning. The positioning error is calculated by comparing the AGV's actual posture at each point in time with the estimated posture of AMCL. Fig. 17 outlines the changes in positioning error across nine instances.



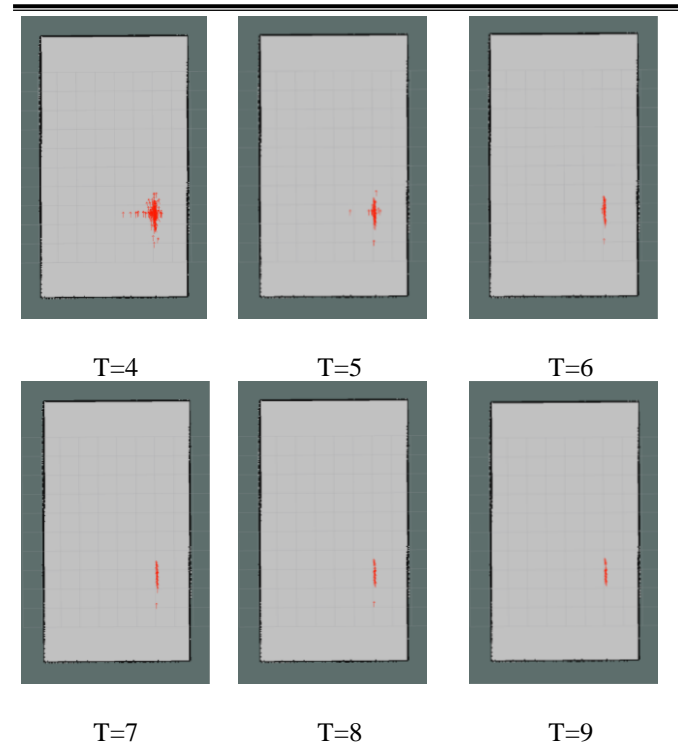


Fig. 16. Particle distribution map of hybrid AMCL/Optical positioning (simulation)

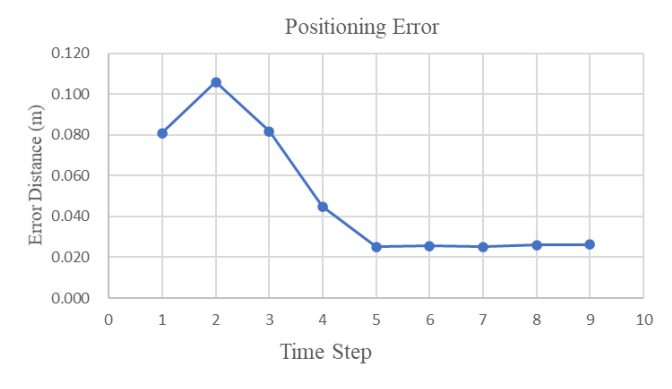


Fig. 17. Hybrid AMCL/Optical positioning error plot

V.EXPERIMENTAL RESULT AND VALIDATION

To assess the performance of the AMCL combined with the optical indoor positioning method, an experimental design equipped with an automated guided vehicle called OmniBot having LiDAR implemented in a planned arena with dimensions of W=1700 mm and L=2900 mm is shown in Fig. 18. The Gmapping SLAM method facilitated map construction, map coordinate system definition, and recording of Corner cube positions. Subsequent experiments involved global indoor positioning, comparing the traditional AMCL method with the AMCL combined with the optical indoor positioning method.

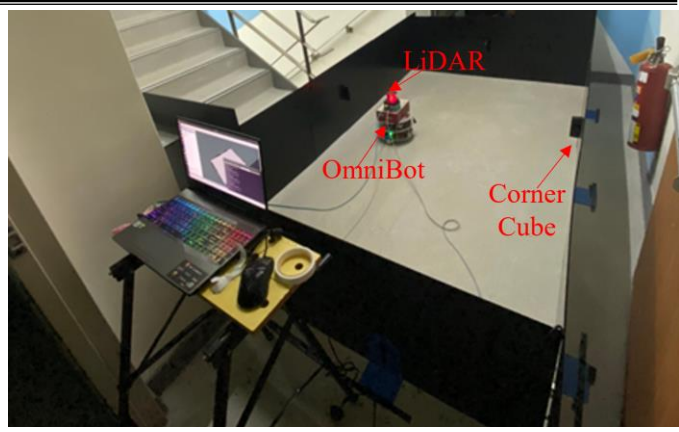


Fig. 18. Experimental test setup

The experimental setup involved reading Omnibot coordinates, AMCL estimated coordinates, and AMCL particle variations from six relay points in a clockwise direction from the bottom left, as shown in Fig. 19. Calculating positioning error values and observing particle convergence, the experiment aimed to verify the global positioning performance of the AMCL combined with the optical indoor positioning method in environments with low characteristics.

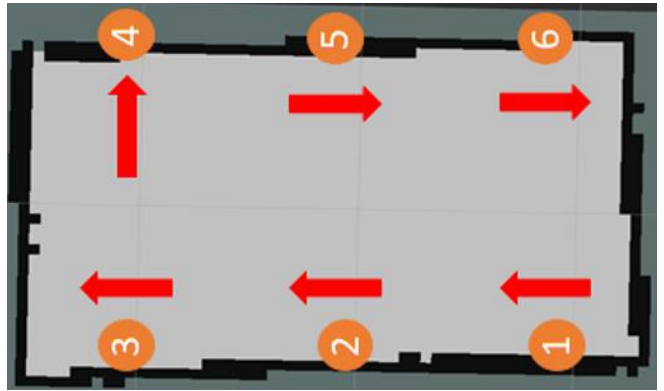
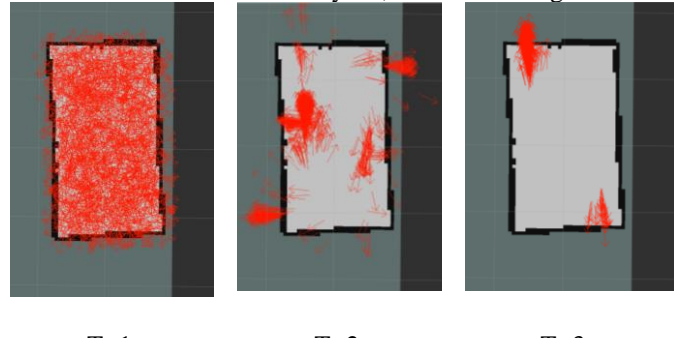


Fig. 19. Positioning relay point

A. Traditional AMCL Results

The method used in this experiment is the traditional AMCL positioning method. The distribution of particles at six different moments is shown in Fig. 20, and the dispersion degree of each particle in the X-axis, Y-axis, and rotation angle around the Z-axis at different times is analyzed, as shown in Fig. 21.



T=1T=2T=3

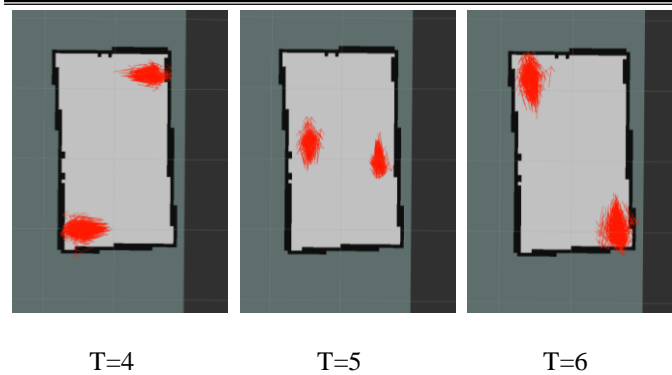
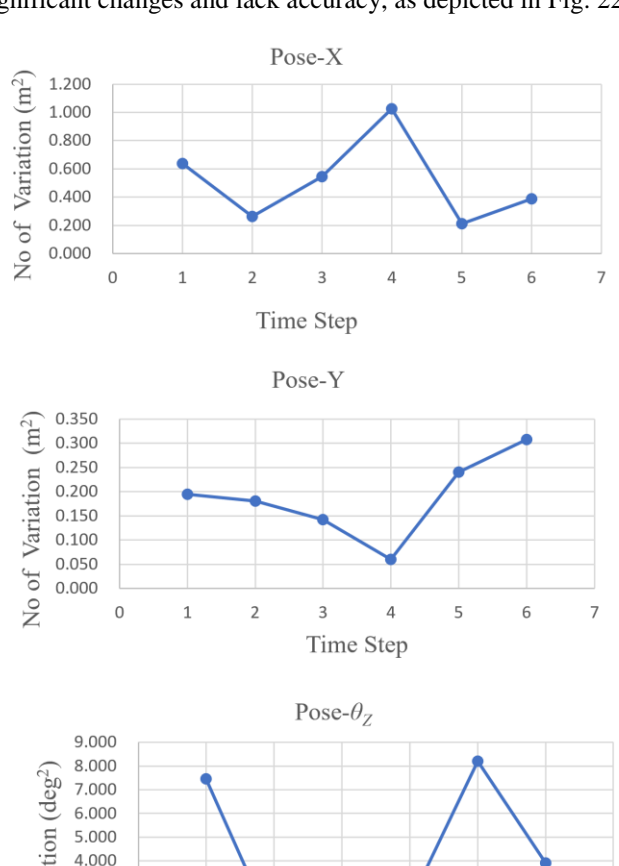


Fig. 20. Particle distribution map for traditional AMCL positioning

Fig. 21 indicates that the particles from the traditional AMCL method do not converge fully after passing through six relay points. Instead, the variation increases in all directions, suggesting challenges in locating within scenes with high feature similarity based solely on lidar signals. The positioning error values, calculated by comparing the actual AGV posture with the estimated AMCL posture at each time point, show significant changes and lack accuracy, as depicted in Fig. 22.



8.000 7.000 90 7.000 100 5.000 110 1.000

Fig. 21. Estimation of pose variation using traditional AMCL positioning

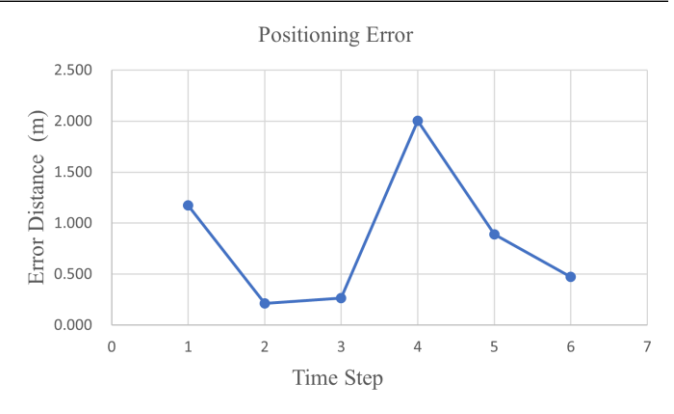


Fig. 22. Traditional AMCL positioning error diagram

B. AMCL Integrated with Optical Indoor Positioning Method

In this analysis, the approach involves AMCL integrated with an optical positioning method. Fig. 23 illustrates the particle distribution at six distinct moments, demonstrating that the AGV can acquire the initial range of possible pose information distributions with the optical positioning method. The analysis focuses on evaluating the dispersion of each particle along the X-axis, Y-axis, and rotational angle around the Z-axis at different times, indicating the variability and distribution of particles in six instances, as presented in Fig. 24.

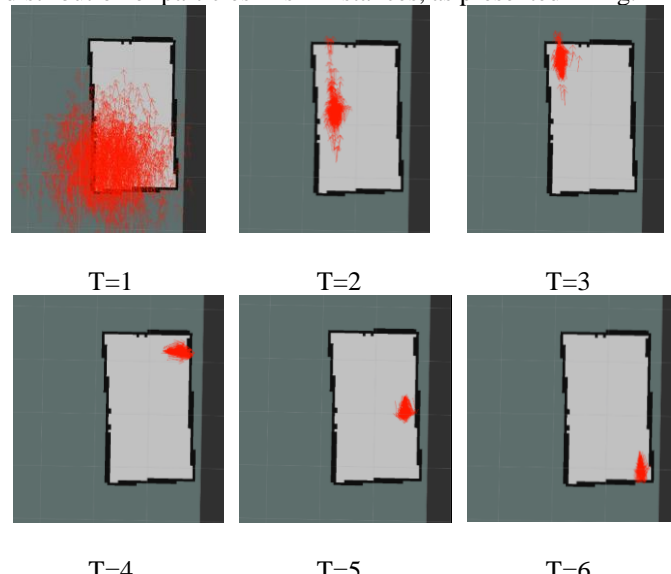
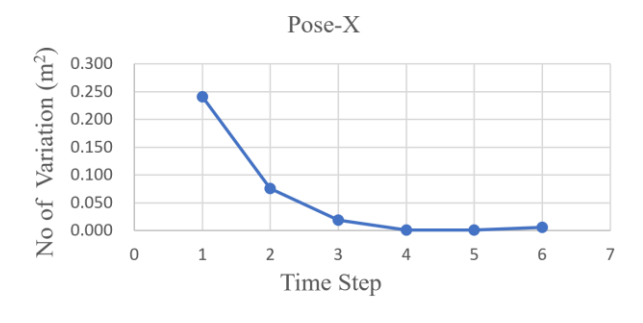
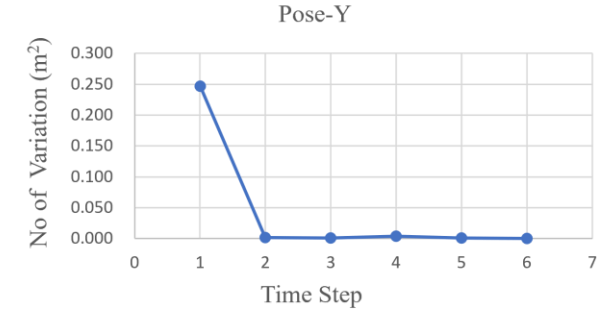


Fig. 23. Particle distribution map for hybrid AMCL-Optical positioning method

Fig. 24 indicates a more concentrated initial particle distribution facilitated by the optical positioning method. Subsequently, through gradual convergence with sensor information during movement, the particles contribute to achieving indoor global positioning. The calculation of positioning error, derived from the comparison between the actual AGV posture and the estimated posture of AMCL at each time point, is depicted in Fig. 25. This representation of positioning error showcases strong accuracy at the onset of global positioning, followed by continuous tracking of the AGV posture state through particle convergence in subsequent instances.





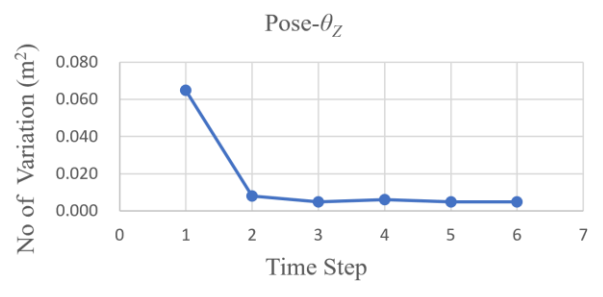


Fig. 24. Estimation of pose variation using hybrid AMCL-Optical positioning method

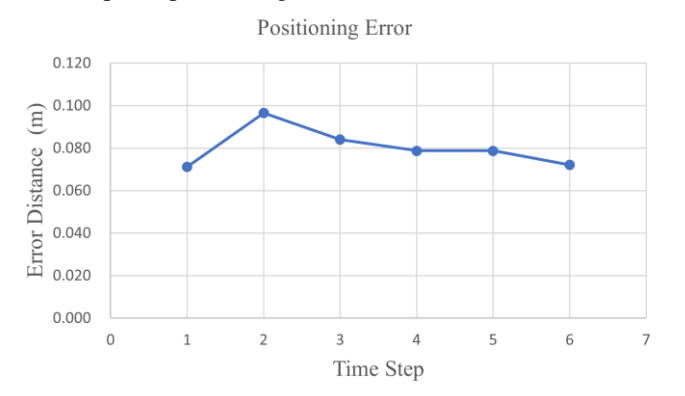


Fig. 25. Hybrid AMCL-Optical positioning error diagram

Examining the Omnibot AGV measurements reveals that relying solely on the traditional AMCL localization method results in slow or even non-existent particle convergence, leading to localization failures attributed to insufficient information or the recognition of similar features. This investigation employs a hybrid approach, combining optical localization with the AMCL method. This integration allows the assignment of particles closely aligned with the AGV's pose. This combined method ensures accurate tracking and precise localization with correct initial conditions.

VI. CONCLUSION

In this study, optical positioning experiments were conducted using LiDAR and Corner Cube based on the polygonal positioning principle. The results indicate that when the LiDAR position is perpendicular to the corner cube, the positioning accuracy is excellent, and the sample size minimally affects accuracy. Even with an angle between the LiDAR and the corner cube, the positioning accuracy slightly decreases in experiments with a small sample size but remains within an acceptable range. Additionally, successful LiDAR SLAM mapping was achieved in this study. Using ROS, traditional AMCL positioning was compared with AMCL combined with optical positioning methods. Results revealed that traditional AMCL localization in featureless environments may lead to localization failure due to particle convergence issues. However, the introduction of optical localization enhances particle convergence, accelerating the overall convergence speed and ensuring successful indoor global positioning. In the future extension of this study, the hybrid method will be implemented in real-time on industrial AGVs for indoor positioning.

ACKNOWLEDGMENT

The support from the National Science and Technology Council, Taiwan (grant number NSTC 112-2811-E011-032, NSTC 112-2218-E-011-009) and Intelligent Manufacturing Innovation Center (IMIC), which is a Featured Areas Research Center in Higher Education Sprout Project of Ministry of Education (MOE), Taiwan (since 2023) were appreciated.

REFERENCES

- [1] M. Wollschlaeger, T. Sauter, and J. Jasperneite, "The future of industrial communication: Automation networks in the era of the internet of things and industry 4.0," *IEEE industrial electronics magazine*, vol. 11, no. 1, pp. 17-27, 2017.
- [2] B. A. Yilma, H. Panetto, and Y. Naudet, "A meta-model of cyber-physical-social system: The cpss paradigm to support human-machine collaboration in industry 4.0," in Collaborative Networks and Digital Transformation: 20th IFIP WG 5.5 Working Conference on Virtual Enterprises, PRO-VE 2019, Turin, Italy, September 23–25, 2019, Proceedings 20, 2019: Springer, pp. 11-20.
- [3] B. Patel, Y. C. Lin, H. J. E. Tong, C.-L. Yang, C.-Y. Chang, and P. T. Lin, "Robot Arm Path Planning with Adaptive Obstacle Avoidance for Man–Robot Collaboration," *Automatic Control and Computer Sciences*, vol. 57, no. 5, pp. 423-438, 2023.
- [4] V. Jaiganesh, J. D. Kumar, and J. Girijadevi, "Automated guided vehicle with robotic logistics system," *Procedia Engineering*, vol. 97, pp. 2011-2021, 2014.
- [5] A. Loganathan and N. S. Ahmad, "A systematic review on recent advances in autonomous mobile robot navigation," *Engineering Science and Technology, an International Journal*, vol. 40, p. 101343, 2023.
- [6] H. Chu, Y. Zhang, J. Xiao, S. Zi, and W. Wang, "An overview location navigation and path planning for automated guided vehicle," in AIIPCC 2021; The Second International Conference on Artificial Intelligence, Information Processing and Cloud Computing, 2021: VDE, pp. 1-6.
- [7] T. Pitkäaho, T. Kaarlela, S. Pieskä, and S. Sarlin, "Indoor positioning, artificial intelligence and digital twins for enhanced robotics safety," *IFAC-PapersOnLine*, vol. 54, no. 1, pp. 540-545, 2021.
- [8] S. Hayward, K. van Lopik, C. Hinde, and A. West, "A survey of indoor location technologies, techniques and applications in industry," *Internet of Things*, p. 100608, 2022.

- [9] M. A. Niloy et al., "Critical design and control issues of indoor autonomous mobile robots: A review," *IEEE Access*, vol. 9, pp. 35338-35370, 2021.
- [10] A. Drira, "GPS navigation for outdoor and indoor environments," University of Tennessee, Knoxville, 2006.
- [11] R. Otero, S. Lagüela, I. Garrido, and P. Arias, "Mobile indoor mapping technologies: A review," *Automation in Construction*, vol. 120, p. 103399, 2020.
- [12] N. El-Sheimy and Y. Li, "Indoor navigation: State of the art and future trends," *Satellite Navigation*, vol. 2, no. 1, pp. 1-23, 2021.
- [13] J. Zhao, S. Liu, and J. Li, "Research and Implementation of Autonomous Navigation for Mobile Robots Based on SLAM Algorithm under ROS," Sensors, vol. 22, no. 11, p. 4172, 2022.
- [14] F. Zafari, A. Gkelias, and K. K. Leung, "A survey of indoor localization systems and technologies," *IEEE Communications Surveys & Tutorials*, vol. 21, no. 3, pp. 2568-2599, 2019.
- [15] W. Cui, Q. Liu, L. Zhang, H. Wang, X. Lu, and J. Li, "A robust mobile robot indoor positioning system based on Wi-Fi," *International Journal of Advanced Robotic Systems*, vol. 17, no. 1, p. 1729881419896660, 2020.
- [16] S. Liu et al., "Development of indoor positioning system based on Bluetooth," in 2021 WRC Symposium on Advanced Robotics and Automation (WRC SARA), 2021: IEEE, pp. 30-35.
- [17] W. A. Cahyadi, Y. H. Chung, and T. Adiono, "Infrared indoor positioning using invisible beacon," in 2019 Eleventh International Conference on Ubiquitous and Future Networks (ICUFN), 2019: IEEE, pp. 341-345.
- [18] F. Che, Q. Z. Ahmed, P. I. Lazaridis, P. Sureephong, and T. Alade, "Indoor Positioning System (IPS) Using Ultra-Wide Bandwidth (UWB)—For Industrial Internet of Things (IIoT)," Sensors, vol. 23, no. 12, p. 5710, 2023.
- [19] Q. Zou, Q. Sun, L. Chen, B. Nie, and Q. Li, "A comparative analysis of LiDAR SLAM-based indoor navigation for autonomous vehicles," *IEEE Transactions on Intelligent Transportation Systems*, vol. 23, no. 7, pp. 6907-6921, 2021.
- [20] S. Yang, L. Ma, S. Jia, and D. Qin, "An improved vision-based indoor positioning method," *IEEE Access*, vol. 8, pp. 26941-26949, 2020
- [21] D. Dardari, P. Closas, and P. M. Djurić, "Indoor tracking: Theory, methods, and technologies," *IEEE Transactions on Vehicular Technology*, vol. 64, no. 4, pp. 1263-1278, 2015.
- [22] M. Regus, R. Talar, and R. Labudzki, "Indoor positioning and navigation system for autonomous vehicles based on RFID technology," in *IOP conference series: materials science and engineering*, 2019, vol. 659, no. 1: IOP Publishing, p. 012059.
- [23] H. Liu, H. Darabi, P. Banerjee, and J. Liu, "Survey of wireless indoor positioning techniques and systems," *IEEE Transactions on Systems, Man, and Cybernetics, Part C (Applications and Reviews)*, vol. 37, no. 6, pp. 1067-1080, 2007.
- [24] J. Rodas, T. M. Fernández, D. I. Iglesia, and C. J. Escudero, "Multiple antennas bluetooth system for rssi stabilization," in 2007 4th International Symposium on Wireless Communication Systems, 2007: IEEE, pp. 652-656.
- [25] A. Pin, "Time of Arrival and Angle of Arrival Estimation of LTE Signals for Positioning Applications," 2020.
- [26] R. Ramirez, C.-Y. Huang, C.-A. Liao, P.-T. Lin, H.-W. Lin, and S.-H. Liang, "A practice of BLE RSSI measurement for indoor positioning," *Sensors*, vol. 21, no. 15, p. 5181, 2021.
- [27] X. Li, Z. D. Deng, L. T. Rauchenstein, and T. J. Carlson, "Contributed Review: Source-localization algorithms and applications using time of arrival and time difference of arrival measurements," *Review of Scientific Instruments*, vol. 87, no. 4, 2016
- [28] J.-R. Jiang, H. Subakti, and H.-S. Liang, "Fingerprint feature extraction for indoor localization," *Sensors*, vol. 21, no. 16, p. 5434, 2021
- [29] A. B. Adege, H.-P. Lin, G. B. Tarekegn, Y. Y. Munaye, and L. Yen, "An indoor and outdoor positioning using a hybrid of support vector machine and deep neural network algorithms," *Journal of sensors*, vol. 2018, pp. 1-12, 2018.
- [30] A. Christy Jeba Malar and G. Kousalya, "Fingerprint-Based Support Vector Machine for Indoor Positioning System," in Smart Innovations in Communication and Computational Sciences: Proceedings of ICSICCS 2017, Volume 2, 2019: Springer, pp. 289-298.

- [31] Z. Wu, J. Liu, and B. Liu, "Particle filter and support vector machine based indoor localization system," *Microsoft Indoor Localization Competition*, Tech. Rep., 2016.
- [32] H. Obeidat, W. Shuaieb, O. Obeidat, and R. Abd-Alhameed, "A review of indoor localization techniques and wireless technologies," *Wireless Personal Communications*, vol. 119, pp. 289-327, 2021.
- [33] A. Morar *et al.*, "A comprehensive survey of indoor localization methods based on computer vision," *Sensors*, vol. 20, no. 9, p. 2641, 2020.
- [34] W. Norzam, H. Hawari, and K. Kamarudin, "Analysis of mobile robot indoor mapping using GMapping based SLAM with different parameter," in *IOP Conference Series: Materials Science and Engineering*, 2019, vol. 705, no. 1: IOP Publishing, p. 012037.
- [35] D. Fox, W. Burgard, F. Dellaert, and S. Thrun, "Monte carlo localization: Efficient position estimation for mobile robots," *Aaai/iaai*, vol. 1999, no. 343-349, pp. 2-2, 1999.
- [36] A. Yilmaz and H. Temeltas, "Self-adaptive Monte Carlo method for indoor localization of smart AGVs using LIDAR data," *Robotics* and Autonomous Systems, vol. 122, p. 103285, 2019.
- [37] P. S. Varma and V. Anand, "Fault-tolerant indoor localization based on speed conscious recurrent neural network using Kullback–Leibler divergence," *Peer-to-peer networking and applications*, vol. 15, no. 3, pp. 1370-1384, 2022.



Pei-Ren Liaw was a M.S. student in the Department of Mechanical Engineering at the National Taiwan University of Science and Technology (NTUST), Taipei, Taiwan.



Brijesh Patel received a Ph.D. degree in Mechanical Engineering from MATS University, India. He is a post-doctoral researcher at the Department of Mechanical Engineering, National Taiwan University of Science and Technology (NTUST), Taiwan. His research interests include robotics, drones, industrial aerodynamics, and composite materials.



Ju-Yi Lee received his M.S. and Ph.D. degree from the Institute of Optoelectronic Engineering, National Chiao Tung University, Taiwan. He is currently a Professor and Chair of the Department of Mechanical Engineering and Director of the Institute of Energy, National Central University (NCU) Taoyuan, Taiwan. His research interests include Optical Metrology, Precise Positioning, and Surface Plasmon Resonance Sensing.



Po Ting Lin received his M.S. and Ph.D. degrees in the Department of Mechanical and Aerospace Engineering at Rutgers University, New Brunswick, New Jersey, USA in 2007 and 2010, respectively. He's currently a Professor in the Department of Mechanical Engineering at National Taiwan University of Science and Technology (NTUST), Taipei, Taiwan. He is the Director of the Global Development Engineering Program (GDEP) and International Advanced Technology Program (IATP) and also the Director of Center for Intelligent Robotics (CIR) at NTUST. His research interests include design optimization with uncertainty, machine vision, industrial robotics, autonomous mobile robots, industry 4.0, cyber-physical systems, etc.